Supercapacitor Electrical and Thermal Modeling, Identification, and Validation for a Wide Range of Temperature and Power Applications

Yasha Parvini, *Student Member, IEEE*, Jason B. Siegel, *Member, IEEE*,
Anna G. Stefanopoulou, *Fellow, IEEE*, and Ardalan Vahidi, *Member, IEEE*

Abstract—**Supercapacitors benefit from unique features including high power density, long cycle life, wide temperature operation range, durability in harsh environments, efficient cycling, and low maintenance cost. This paper presents a validated lumped and computationally efficient electrical and thermal model for a cylindrical supercapacitor cell. The electrical model is a two-state equivalent electric circuit model with three parameters that are identified using temporal experiments. The dependence of the parameters on the state of charge, current direction and magnitude (20–200 A), and temperatures ranging from -40 °C to 60 °C is incorporated in the model. The thermal model is a linear 1-D model with two states. The reversible heat generation which is significant in double-layer capacitors is included in the thermal model. The coupling of the two models enables tuning of the temperature-dependent parameters of the electrical model in real time. The coupled electrothermal model is validated using real-world duty cycles at subzero and room temperatures with root-mean-square errors of (82 mV–87 mV) and (0.17 °C–0.21 °C) for terminal voltage and temperature, respectively. This accurate model is implementable in real-time power applications and also thermal management studies of supercapacitor packs.**

Index Terms—**Electrical model, energy storage, entropic heat generation, identification, supercapacitor, thermal model.**

I. Introduction

ENERGY storage systems vastly facilitate the development of areas such as renewable power generation [1], [2], vehicle electrification [2], and mobile electronic devices. Within different electrical energy storage technologies, *supercapacitors* also known as *ultracapacitors* or *electric double-layer capacitors* (EDLCs) are interesting because of their unique

characteristics and broad application spectrum. Supercapacitors have been utilized in wind power generation for smoothing fast wind-induced power variations [3]–[5]. Examples of supercapacitors functioning as energy buffers in solar power generation via photovoltaic panels and Stirling engines are reported in the literature [6], [7]. Supercapacitors are also used in power system protection as uninterruptible power supply in different fields such as telecommunications [8], [9]. Luo *et al.* present supercapacitors as a promising energy storage for applications in power systems such as transmission and distribution stabilization, voltage regulation and control, and motor starting [10]. In bioengineering, supercapacitors are exploited as energy storage units in medical devices including magnetic resonance imaging and as power supply for laser-based breast cancer detector [11], [12]. In cars, aircraft, and railway vehicles, supercapacitors have been studied both as stand-alone storage modules and in combination with batteries or fuel cells [13]–[17]. In [18], having the high efficiency and fast-charging capability of supercapacitors in mind, an optimal charging current is obtained considering the dynamics of the vehicle and the electric motor during regenerative braking. Another interesting application of supercapacitors is boosting the poor low-temperature performance of batteries and also helping the cold start of engines [19], [20].

A model of a supercapacitor is required in all of the aforementioned applications in order to simulate the performance of the system while satisfying electrical and thermal constraints. Electrical models of supercapacitors can be categorized in two groups: 1) models that attempt to mimic all of the physical and chemical phenomena of charging and discharging which are accurate but not computationally efficient. Continuum models based on Poisson–Nernst–Planck equations, atomistic models based on molecular dynamics, and quantum models based on electron density functional theory are in this category [21], and 2) models that are suitable for system level studies and real-time applications, which are computationally efficient but less accurate than the detailed models in 1) above. In this paper, we are interested in introducing a validated equivalent electric circuit model appropriate for real-time integration at a system level. A number of studies have focused on modeling the electrical behavior of supercapacitors in time and frequency domains by proposing equivalent electric circuit models

and their identification procedure [22]–[24]. Musolino *et al.* propose a full-frequency-range model that captures the self-discharge and redistribution phenomena in supercapacitors [25]. Torregrossa *et al.* improves the model presented in [22] by capturing the diffusion of the supercapacitor residual charges during charging/discharging and rest phases [26]. In [27], Rizoug *et al.* use frequency analysis to identify the resistive parameters and a time domain approach for capacitance characterization. These proposed models are accurate for fixed temperature operations as the dependence of the model parameters on temperature is not taken into account. The importance of the variation of the electrical model parameters with temperature is studied in [28] and [29]. The proposed equivalent circuit model in this paper has the following characteristics:

1) The terminal voltage dynamics are captured with high accuracy (20–87 mV) suitable for all power system applications.
2) Computationally efficient with only three parameters to be identified.
3) The carefully designed temporal experiments (pulse-relaxation) are utilized for identification purposes.
4) The dependence of the model parameters on temperature (range: -40 °C to 60 °C), state of charge (SOC; range: 0–100), current direction (charge/discharge), and also for the first time current magnitude (range: 20–200 A) is investigated.

On the other hand, having the knowledge of how the temperature of a supercapacitor cell varies enables designing cooling management systems at the stack level [30], predicting the aging behavior [31], and real-time tuning of the temperature-dependent parameters of the electrical model [32]. The thermal dynamics can be predicted by numerically solving the governing partial differential equations (PDEs) as investigated in [33] and [34]. However, these complex first principle models are computationally expensive and therefore not suitable for real-time applications. Utilizing a reduced-order thermal model with sufficient accuracy for power applications is of interest in this study. In [35], Berrueta *et al.* propose reduced-order electrical and thermal models for a 48-V supercapacitor module with the application of the electrical model shown in a microgrid case study. However, the thermal model is over simplified by neglecting the reversible heat generation effect which is significant in EDLCs [36] and considering the pack as a whole body (0-D model) which results in a high reported RMS error for the thermal model (2.229 °C) [35]. In [37], electrical and thermal models are proposed, and efforts have been made on including the reversible heat generation; however, clear results on capturing the exothermic effect during charging and endothermic behavior during discharging are not observable in the paper. The proposed reduced-order thermal model in this study has the following characteristics:

1) The thermal model is a linear 1-D model with two states.
2) The temperature dynamics is captured with high accuracy (0.17 °C–0.21 °C) suitable for thermal management systems.
3) Computationally efficient with only four parameters to be identified.

Parameter	Value
Nominal Voltage (V)	2.7
Nominal Capacitance (F)	3000
Mass (Kg)	0.5
Specific Power (WKg^{-1})	5900
Specific Energy (WhKg^{-1})	6

4) Both reversible (entropic effect) and irreversible heat generations (joule heating) are integrated in the model.
5) The real-world duty cycles are used to parameterize the model.
6) The thermal model is coupled with the electrical model to capture the changes in the parameters of the electrical model that depend on temperature.
7) The coupled electrothermal model is validated in both subzero and room temperatures, using a practical duty cycle rather than simple constant current cycles often used in the literature.

The preliminary results of this study were presented in [38], where the focus was on subzero temperatures and high currents. The remainder of this paper is organized in the following order. In Section II, the experimental setup is described. In Section III, the electrical model of the supercapacitor and its parameterization is presented. Section IV describes the thermal model, integration of the reversible heat generation in the model, coupling of the electrical and thermal models, and identification results of the thermal model. Sections V and VI discuss the validation of the electrothermal model and conclusion remarks.

II. EXPERIMENTAL SETUP

Experiments have been conducted on a cylindrical Maxwell BCAP3000 cell with activated carbon as electrodes. The cell contains nonaqueous electrolyte allowing the maximum rated voltage of 2.7 V. The specifications of the cell are listed in Table I. All of the pulse-relaxation experiments related to parameterization and validation of both electrical and thermal models are conducted using the following set of equipment:

1) Power supply: Bitrode FTV1-200/50/2-60 cycler, capable of supplying up to 200 A.
2) Thermal chamber: Cincinnati subzero ZPHS16-3.5-SCT/ AC, capable of controlling the ambient temperatures as low as -40 °C and up to 150 °C.
3) Temperature sensor: OMEGA T-type thermocouple attached to the surface of the cell. The accuracy of this thermocouple is the maximum of 0.5 °C and 0.4%.

The cell is connected to the power supply and horizontally (with respect to the direction of the air flow approaching the cell) suspended inside the thermal chamber to allow uniform air flow around the cell for a better identification of the convective heat coefficient. Within the four thermal parameters to be identified, the convective heat transfer coefficient depends on the cell orientation and the air flow rate around the cells in a pack. Depending of these factors, the identified convective heat transfer coefficient in this study may vary from its value in certain
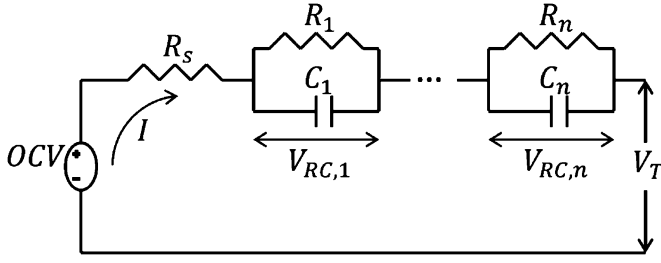
Fig. 1. Schematic of the equivalent electric circuit model with "n" number of $R-C$ branches.

package designs. One solution is to obtain the convective heat transfer coefficient by characterizing the cell for the specific package geometry and cooling conditions.

III. ELECTRICAL MODEL OF THE SUPERCAPACITOR

The equivalent electric circuit model, identifying cell capacitance and open-circuit voltage, and also electric model parameter estimation results are presented in this section.

A. Equivalent Electric Circuit Model

In this paper, the galvanostatic approach is used in the whole modeling procedure where current is the input to the system and the output of interest is the terminal voltage. This approach is also widely used in the battery literature for parameterizing equivalent electric circuit model parameters [39]–[41] and using the model in control-oriented research such as optimal charging of lithium-ion and lead-acid batteries [42]. Fig. 1 shows the schematic of the proposed equivalent electric circuit model. It consists of a resistance R_s connected in series to the $R-C$ branches. Considering a positive sign for charging and a negative sign for discharging and applying Kirchhoff's voltage law to the circuit shown in Fig. 1, the equation governing the terminal voltage V_T could be written as follows:

$$V_T = \text{OCV}(\text{SOC}) + IR_s + \sum_{j=1}^{n} V_{RC,j}. \tag{1}$$

In (1), OCV is the open-circuit voltage which is a linear function of SOC for an ideal capacitor. The SOC is determined by coulomb counting by the following state equation:

$$\frac{d\text{SOC}}{dt} = \frac{I}{CV_{\max}} \tag{2}$$

where C and $V_{\max}$ are the nominal capacitance in farads and the maximum voltage across the cell at full charge. The second term in (1) is the voltage drop over the series resistance, and the last part is the sum of voltage drops across $R-C$ branches. Dynamics of each $R-C$ pair is described as:

$$\frac{dV_{RC,j}}{dt} = -\frac{1}{R_j C_j} V_{RC,j} + \frac{I}{C_j} \tag{3}$$

where R_j and C_j are the corresponding resistance and capacitance of each $R-C$ branch, respectively.

B. Cell Capacitance and Open-Circuit Voltage

The open-circuit voltage OCV and capacitance C are the primary modeling parameters to be identified. Capacitance and capacity are the terms used to determine the amount of electric charge stored in electrical energy storage systems. Capacitance is the term used for supercapacitors with the unit of farads. Equivalently, the term capacity is used in the battery literature with the unit of ampere hours (Ah). The relationship between capacity in Ah and capacitance (C) in farads is:

$$\text{capacity} = \frac{CV_{\max}}{3600}. \tag{4}$$

The capacitance of the cell used in this study is 3000 F, which is equivalent to 2.25 Ah. The term C-rate is the rate at which charging (discharging) is performed. For example, charging a cell with a capacity of 2.25 Ah from 0 to full charge with a C-rate of 1 means supplying a current of 2.25 A that results in a charging time of 1 h. Similarly, the charging current values used in this study, which are 22.5, 67.5, 135, and 191 A, are equivalent to C-rates of 10 C, 30 C, 60 C, and 85 C, respectively. The power supply utilized in this research has a current limit of 200 A, which is the reason of choosing 191 A as the maximum pulse current applied in the experiments. The capacitance is obtained by charging the cell from 0 to maximum voltage by applying a small constant current. The reason for using a small current is to minimize the effect of resistive losses and measure the capacitance more accurately. Constant current assumption allows us to integrate (2) using the boundary conditions $\text{SOC}(0) = \text{SOC}_i$ and $\text{SOC}(t_f) = \text{SOC}_f$ and to find the capacitance:

$$C = \frac{t_f I(t)}{V_{\max}(\text{SOC}_f - \text{SOC}_i)} \tag{5}$$

where t_f is the charging time. SOC_f and SOC_i are not measured and, by definition, are 1 at full charge ($V_T = V_{\max} = 2.7$ V) and 0 at the empty state ($V_T = V_{\min} = 0$ V). The charging current used in the experiment was 0.112 A (equivalent to a C-rate of $C/20$), and the time recorded to fully charge the empty cell was 21.05 h, which, according to (5), results in a capacitance of 3143 F. Similarly, a constant current of 0.1178 A was applied to discharge the fully charged cell to 0. The recorded time was 18.73 h, resulting in a capacitance of 2934 F. The reported nominal capacitance by the manufacturer is 3000 F, which is almost the average of the measured capacitance for charging and discharging. The OCV as a function of SOC is obtained by charging the cell from $V_0 = 0$ V to $V_{\max} = 2.7$ V with a small constant current of 0.45 A (equivalent to a C-rate of $C/5$). By applying a small constant current, the recorded terminal voltage at each time corresponds to the OCV at that time. The obtained OCV profile is almost identical for a C-rate equal to $C/5$ compared to $C/20$, so we present the results based on the $C/5$ rate, which is a shorter test to run. Using the coulomb counting method governed by (2), SOC is obtained at each time. This provides a profile for OCV as a function of SOC to be integrated in the supercapacitor model. The difference between charging and discharging OCV is small due to the low current and small equivalent series resistance. The OCV as a function of SOC is shown in Fig. 2. In this figure, the ideal linear OCV,
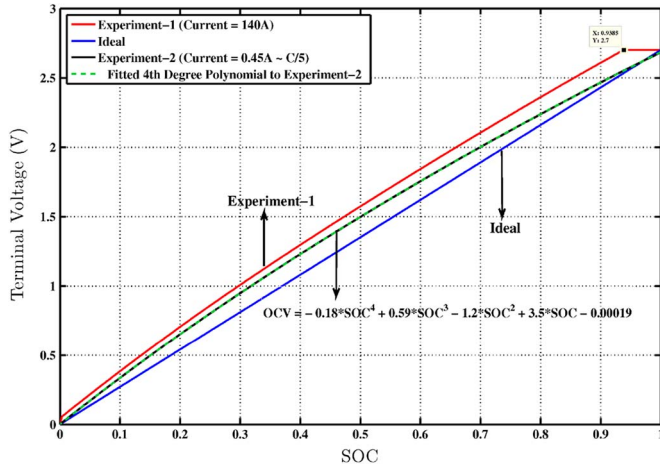
Fig. 2. Ideal and real OCVs for low and high currents versus SOC.

Fig. 3. Sample pulse-relaxation test at 25 °C and 191 A of current.

Fig. 4. R_s as a function of SOC for all temperatures and at each pulse current level during discharging.

the measured terminal voltage with a high constant current of 140 A, and the OCV used in this study are shown. The effect of high current is shown to compare it with the low current measurements. As it can be observed, the high current results in a loss of capacity of 6% as the cell reaches its maximum allowed voltage in a shorter time. This is the reason of using low current for identifying the capacity and the OCV of the cell. The open-circuit voltage of the supercapacitor under investigation has a nonlinear relationship with SOC as shown in experiment-2 in Fig. 2. A fourth-order polynomial is fitted to the OCV versus SOC data and integrated in the model as follows:

$$\text{OCV(SOC)} = -0.18(\text{SOC})^4 + 0.59(\text{SOC})^3 - 1.2(\text{SOC})^2 \\ + 3.5(\text{SOC}) - 1.9 \times 10^{-4}. \quad (6)$$

The nonlinearity in the OCV profile is due to the small pseudo-capacity behavior of the cell [43].

C. Equivalent Electric Circuit Model Identification

The unknown parameters of the equivalent circuit are R_s, R_j, and C_j. In order to record a rich set of data for identification and also to investigate the dependence of the parameters on SOC, current magnitude and direction, and also temperature, the following set of pulse-relaxation experiments is performed:

1) Experiments are conducted at six temperature levels (-40 °C, -20 °C, 0 °C, 25 °C, 40 °C, and 60 °C). The lower and upper limits for the temperature are the actual limits reported by the manufacturer.
2) At each temperature level, four pulse current rates (191, 135, 67.5, and 22.5 A) are applied.
3) Starting at a fully discharged state, the cell is charged by the constant pulse current up to 5% SOC. Next, a 20 seconds relaxation period begins by cutting the current. This procedure is repeated for each 5% SOC increment until the cell is fully charged.
4) Similar pulse-relaxation procedure is repeated for discharging immediately at the end of the charging process.

Fig. 3 is one example of the total of 24 different pulse-relaxation tests. This test will be called the *sample test* through-
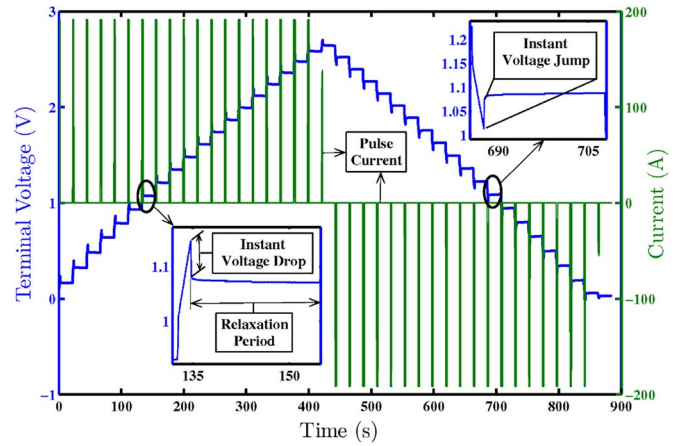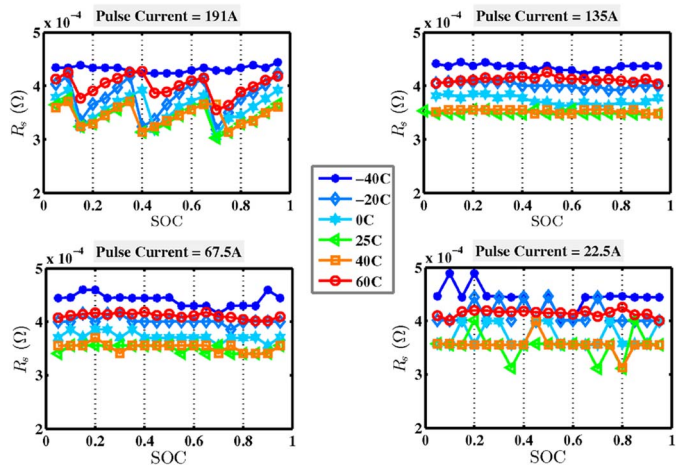
out this paper and will be used to present the identification process and model accuracy investigation. In this specific test, the temperature is 25 °C, and the current is 191 A.

The relaxation period at each SOC level contains the information needed to estimate the equivalent electric circuit model parameters. The relaxation or rest phase consists of two segments as depicted by the insets in Fig. 3. The first part is a sudden change in terminal voltage at the moment the current is set to 0. This change is observed by an instant drop in voltage while charging and a jump in voltage during discharge. This behavior is captured by R_s in the model. The second part in the relaxation stage is the exponential behavior in voltage and is modeled by the $R-C$ branches. R_s is obtained by dividing the instant voltage change by the pulse current at each 5% SOC level.

Fig. 4 illustrates the variation of R_s during discharge with respect to SOC and temperature at each current level. This figure shows that, as the temperature increases, R_s decreases regardless of the current magnitude, except for 60 °C. In supercapacitors, the electronic resistance of the electrode and electrolyte and also the interfacial resistance between the electrode and the current collector contribute to the amount of R_s [44], where an increase in these resistances could contribute to the increase in R_s at 60 °C. The dependence of R_s on SOC is small
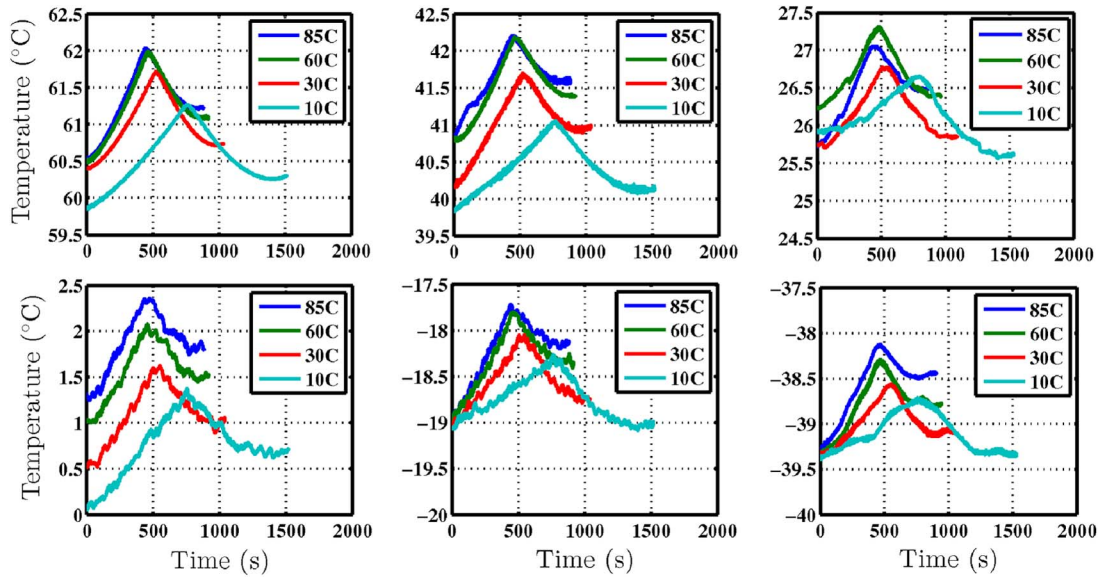
Fig. 5. Supercapacitor cell surface temperature at different ambient temperatures and pulse current rates.

according to Fig. 4 for all temperatures and currents, except the high-current case (191 A). The power supply's current sensor accuracy is 0.1% in full scale (current = 200 A). Therefore, the measurement error is less than or equal to ± 200 mA. For example, the variance calculated for the measured constant current of 140 A is 2.1E−3 A^2, equal to a standard deviation of 45 mA. This results in a small variation of ± 0.1 $\mu\Omega$ in the estimated value for R_s at 135 A and 25 °C. The R_s values obtained in other experiments are also within similar range of accuracy.

The temperature measurements from the thermocouple attached to the surface of the cell for all 24 sets of pulse-relaxation tests are depicted in Fig. 5. This figure shows that applying a higher pulse current results in a higher surface temperature at the end of the charging period regardless of the ambient temperature. The highest observed increase in surface temperature is 1.5 °C at the highest ambient temperature of 60 °C and at the highest current of 191 A. According to Fig. 4, a 23%–30% increase in R_s occurs from 40 °C to -40 °C. This indicates that the effect of a small change in temperature during the pulse-relaxation tests on R_s is negligible. Another interesting observation from Fig. 5 is that, during discharging, the surface temperature of the cell decreases. This phenomenon and the reasoning will be addressed in the thermal modeling section of this paper.

At this point, the knowledge of the small variation of R_s with SOC and negligible temperature effect during each pulse-relaxation test allows us to consider a constant value for R_s at each temperature and current level. This is done by taking the average of R_s with respect to SOC for the charging and discharging sections separately. The final R_s is obtained by averaging the values obtained from the charging and discharging sections for each pulse-relaxation test. Fig. 6 shows the variation of the average R_s with temperature and current magnitude. This figure indicates that R_s is highest at -40 °C and that the change of the average R_s with respect to temperature is higher than that due to the current magnitude. The resistances contributing to the amount of R_s are the electronic
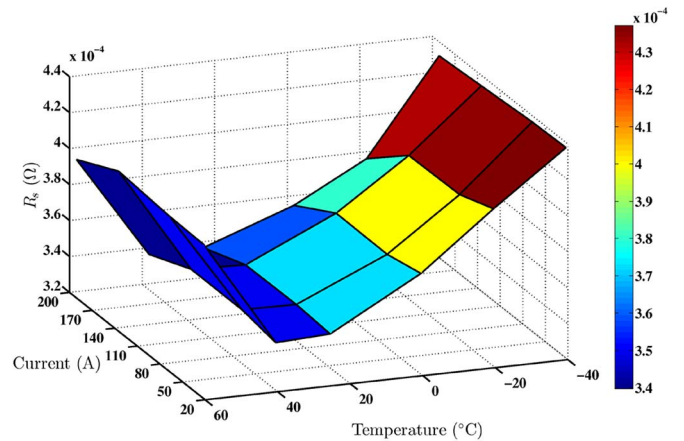

Fig. 6. Measured average R_s as a function of temperature and current.

resistance of the electrode material, resistance between the electrode and the current collector, electrolyte resistance, and ionic resistance of ions moving through the separator [45]. The dependence of R_s on the electrode and electrolyte resistance is investigated in [46], showing that the lower amount of the active carbon material used in the electrode and also higher electrolyte conductivity will result in a smaller R_s. The effect of the resistance between the electrode material and the current collector is studied in [44], illustrating that treating the current collector before applying the coating of active carbon will result in a smaller R_s. The lower R_s at higher temperature is due to the decrease in the electronic resistance of the electrode and electrolyte resistance [45], [46]. Fig. 6 also shows that the change of R_s with respect to the current is small and could be considered constant at each temperature level.

The next step is to identify the values of the resistance and capacitance of the $R-C$ branches with the assumption that the parameters are constant and not a function of SOC. Identification of R_j and C_j is performed by minimizing the square error between the measured and simulated terminal voltages

TABLE II
RMSE BETWEEN THE MODEL AND THE EXPERIMENT

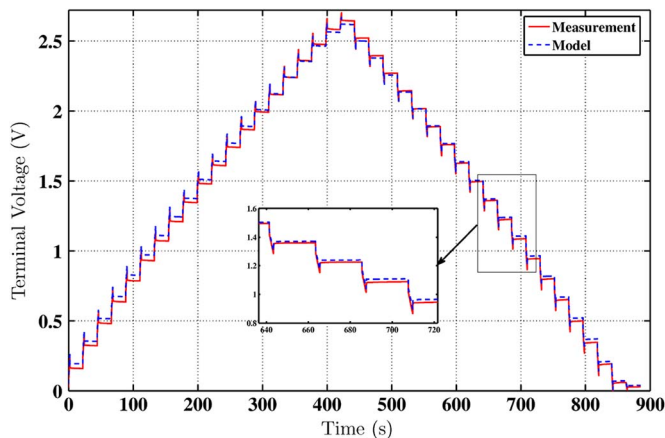| Model	RMSE (mV)
Linear-OCV-R_s	100
Nonlinear-OCV-R_s	50
OCV-R_s-RC	20

Fig. 7. Comparison between terminal voltages from the experiments and the $OCV - R_s - $ RC model for the sample test.

for each pulse-relaxation experiment to obtain the estimated values for each temperature level and current magnitude. The cost function to be minimized is

$$J = \sum_k \left(V_m(k) - V_T(k) \right)^2 \qquad (7)$$

where V_m and V_T are the measured and simulated terminal voltages, respectively. The number of $R-C$ branches will be determined based on the accuracy of the parameterized models. First, a simple first-order model named $OCV - R_s$, which consists of a resistance R_s connected in series to the terminals of the supercapacitor, is considered. The single parameter in this model is R_s, which is already identified. The root-mean-square error (RMSE) between the modeled terminal voltage and the sample test experiment, considering the ideal versus the real OCV (according to (6)), is obtained. The RMSE numbers in Table II show that the real nonlinear OCV profile should be integrated in the model as the results for the sample test indicate a 50% decrease in RMS error compared to using the ideal OCV in the model. The drop in RMSE is also significant for the other tests, using the nonlinear OCV profile. In the next step, a single $R-C$ branch is added in series to the $OCV - R_s$ to build the $OCV - R_s - RC$ model. Fig. 7 compares the terminal voltage results from the $OCV - R_s - RC$ model and the experimental data from the sample test. The result shows that the electrical model with the estimated R_1 and C_1 accurately predicts the dynamics of the terminal voltage with an RMSE of 20 mV as listed in Table II.

This result shows that the $OCV - R_s - RC$ model is accurate enough, and it will be used as the final electrical model. By performing a similar procedure used to estimate the electric model parameters for the sample test, R_1 and C_1 were also identified for the remaining 23 pulse-relaxation experiments.
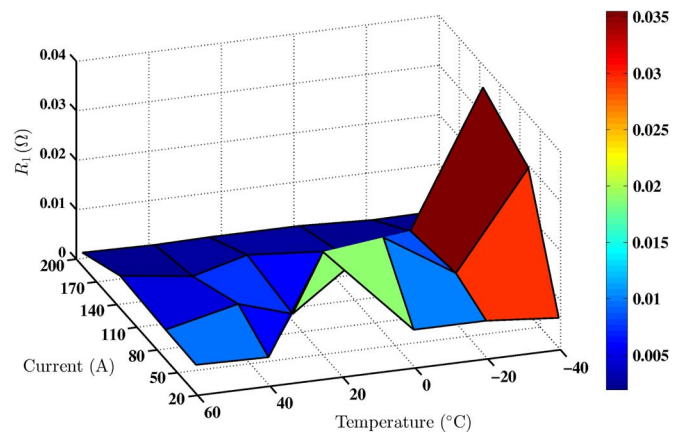

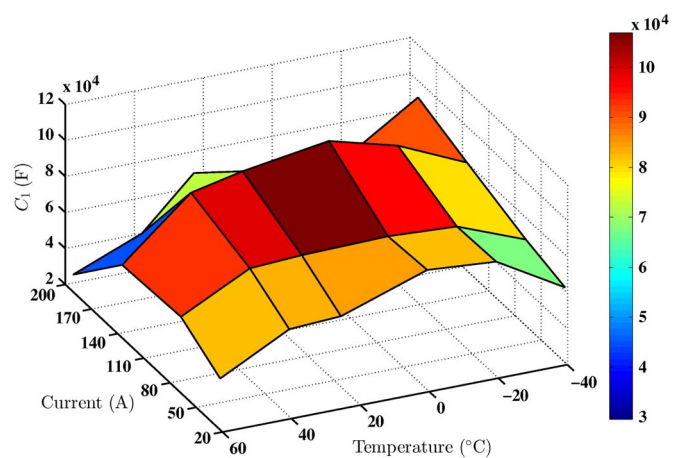Fig. 8. Estimated R_1 as a function of temperature and current.

Fig. 9. Estimated C_1 as a function of temperature and current.

Figs. 8 and 9 summarize the estimated parameters, R_1 and C_1, as a function of all temperature and current levels. The resistance in the $R-C$ branch represents the polarization resistance which, in general, is due to the kinetic reactions and also the diffusion process. In the case of a double-layer supercapacitor with carbon electrodes and organic electrolyte, the kinetic reactions are minimum. The charge transfer is mostly based on electrostatic diffusion of ions in the pores of the electrode material. Similar to R_s that reaches its maximum value at low temperatures, R_1 also shows such a behavior. The C_1 value corresponds to the double-layer capacitance of the supercapacitor. The value of C_1 depends on the surface area of the activated carbon, the electrical conductivity of the electrolyte, and the double-layer effective thickness [28], [47]. The variation of any of the mentioned parameters contributes to the observed higher value of C_1 at the current of 135 A. One direction for future work is to use a more complicated model and also *in situ* measurements to explain the current dependence of model parameters in detail.

IV. THERMAL MODEL OF THE SUPERCAPACITOR

A computationally efficient thermal model developed for cylindrical batteries [48] is modified and adopted for the thermal modeling of the supercapacitor. In the beginning of this
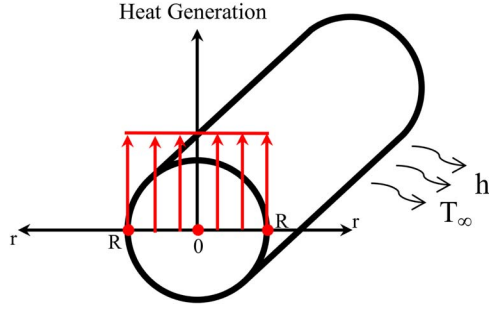
Fig. 10. Given the assumption of uniform heat generation with a convective cooling boundary condition at the surface, the radial temperature distribution can be modeled as a fourth-order polynomial.

section, the two-state thermal model will be described. In the consecutive sections, entropic heat generation and electrothermal coupling will be introduced. Finally, parameterization results are presented.

A. Two-State Thermal Model

The model is based on 1-D heat transfer along the radial direction of a cylinder, with convective heat transfer boundary conditions as illustrated in Fig. 10. A cylindrical supercapacitor, the so-called jelly roll, is fabricated by rolling a stack of cathode/separator/anode layers. Assuming a symmetric cylinder, constant lumped thermal properties such as cell density, conduction heat transfer, and specific heat coefficient are used [48]. Uniform heat generation along the radial direction is a reasonable assumption according to [49]. The temperature distribution in the axial direction is more uniform than the radial direction due to higher thermal conductivity [50]. The radial 1-D temperature distribution is governed by the following PDE:

$$\rho c_p \frac{\partial T(r,t)}{\partial t} = k_t \frac{\partial^2 T(r,t)}{\partial r^2} + \frac{k_t}{r} \frac{\partial T(r,t)}{\partial r} + \frac{Q(t)}{V_{\text{cell}}} \quad (8)$$

with boundary conditions

$$\left. \frac{\partial T(r,t)}{\partial r} \right|_{r=0} = 0 \quad (9)$$

$$\left. \frac{\partial T(r,t)}{\partial r} \right|_{r=R} = -\frac{h}{k_t}(T(R,t) - T_\infty) \quad (10)$$

where t, ρ, c_p, and k_t are time, volume-averaged density, specific heat, and conduction heat transfer coefficients, respectively. The heat generation rate inside the cell is Q, the cell volume is V_{cell}, and R is the radius of the cell. The first boundary condition in (9) is to satisfy the symmetric structure of the cell around the core. The convective heat transfer at the surface of the cell forms the boundary condition in (10). Here, T_∞ is the ambient air temperature, and h is the heat transfer coefficient for convective cooling. With uniform heat generation distribution as depicted in Fig. 10, the solution to (8) is assumed to satisfy the following polynomial temperature distribution as proposed in [51]:

$$T(r,t) = \alpha_1(t) + \alpha_2(t)\left(\frac{r}{R}\right)^2 + \alpha_3(t)\left(\frac{r}{R}\right)^4. \quad (11)$$

The volume-averaged temperature $\bar{T}$ and volume-averaged temperature gradient $\bar{\gamma}$ are chosen as the states of the thermal model. These quantities can be related to the temperature distribution as follows:

$$\bar{T} = \frac{2}{R^2}\left[\int_0^R rT\,dr\right] \quad (12)$$

$$\bar{\gamma} = \frac{2}{R^2}\left[\int_0^R r\left(\frac{\partial T}{\partial r}\right)dr\right]. \quad (13)$$

The time-varying parameters $\alpha_1(t)$, $\alpha_2(t)$, and $\alpha_3(t)$ can be solved as a function of $\bar{T}$, $\bar{\gamma}$, and $T_s = T(R,t)$. Substituting these obtained values in (11), $T(r,t)$ is written as a function of the states and surface temperature as follows:

$$T(r,t) = 4T_s - 3\bar{T} - \frac{15R}{8}\bar{\gamma}$$
$$+ \left[-18T_s + 18\bar{T} + \frac{15R}{2}\bar{\gamma}\right]\left(\frac{r}{R}\right)^2$$
$$+ \left[15T_s - 15\bar{T} - \frac{45R}{8}\bar{\gamma}\right]\left(\frac{r}{R}\right)^4. \quad (14)$$

At this point, the obtained expression for $T(r,t)$ is substituted in the following two integral equations that are based on the PDE in (8):

$$\int_0^R \left[\rho c_p \frac{\partial T(r,t)}{\partial t} - k_t \frac{\partial^2 T(r,t)}{\partial r^2} - \frac{k_t}{r}\frac{\partial T(r,t)}{\partial r} - \frac{Q(t)}{V_{\text{cell}}}\right]dr = 0$$

$$\int_0^R \frac{\partial}{\partial r}\left[\rho c_p \frac{\partial T(r,t)}{\partial t} - k_t \frac{\partial^2 T(r,t)}{\partial r^2} - \frac{k_t}{r}\frac{\partial T(r,t)}{\partial r} - \frac{Q(t)}{V_{\text{cell}}}\right]dr = 0.$$

These algebraic operations reduce the PDE to a set of two linear ordinary differential equations with the state space representation of:

$$\dot{x} = Ax + Bu \quad y = Cx + Du \quad (15)$$

where $x = [\bar{T} \quad \bar{\gamma}]^T$, $u = [Q \quad T_\infty]^T$, and $y = [T_c \quad T_s]^T$ are the state, input, and output vectors, respectively. The two outputs of the model are the surface temperature T_s and core temperature T_c. The parameter $\beta = k_t/\rho c_p$ is the thermal diffusivity. Finally, the linear system matrices A, B, C, and D are:

$$A = \begin{bmatrix} \dfrac{-48\beta h}{R(24k_t + Rh)} & \dfrac{-15\beta h}{24k_t + Rh} \\ \dfrac{-320\beta h}{R^2(24k_t + Rh)} & \dfrac{-120\beta(4k_t + Rh)}{R^2(24k_t + Rh)} \end{bmatrix}$$

$$B = \begin{bmatrix} \dfrac{\beta}{k_t V_{\text{cell}}} & \dfrac{48\beta h}{R(24k_t + Rh)} \\ 0 & \dfrac{320\beta h}{R^2(24k_t + Rh)} \end{bmatrix}$$

$$C = \begin{bmatrix} \dfrac{24k_t - 3Rh}{24k_t + Rh} & -\dfrac{120Rk_t + 15R^2 h}{8(24k_t + Rh)} \\ \dfrac{24k_t}{24k_t + Rh} & \dfrac{15Rk_t}{48k_t + 2Rh} \end{bmatrix}$$

$$D = \begin{bmatrix} 0 & \dfrac{4Rh}{24k_t + Rh} \\ 0 & \dfrac{Rh}{24k_t + Rh} \end{bmatrix}.$$
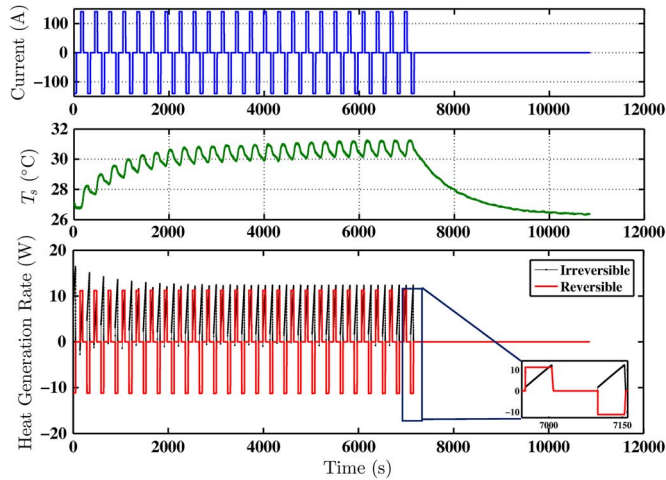
Fig. 11. Reversible and irreversible heat generation rates for a test at 25 °C, 140 A, 90 seconds rest, and full SOC range.

This linear two-state model is relatively easier to parameterize compared to the detailed PDE model, as shown in the following sections.

B. Thermal Test Procedure

In order to investigate the dependence of temperature dynamics on current magnitude, depth of discharge (SOC range), and also relaxation period (rest time), the following set of repeated cycling experiments is performed.

1) Experiments are conducted at two temperature levels (-20 °C and 25 °C).
2) At each temperature level, three current levels (140, 100, and 50 A) are applied.
3) Two SOC ranges (0%–100% and 50%–100%) and two resting times (90 seconds and 0 seconds) are studied.
4) In each set of experiments, a fully discharged or a half-charged cell undergoes cycles of charge–rest–discharge until the surface temperature of the cell reaches steady state. This is followed by a long rest period until the surface temperature relaxes to its initial value.

C. Irreversible and Reversible Heat Generation

The total heat generation consists of two parts. The first contributor to the total heat generation is the ohmic losses, which is responsible for the overall increase in temperature observable in Fig. 11. These losses are due to the internal resistance of the cell. This irreversible joule heating effect is associated with the losses in R_s and R_1 as follows:

$$Q_{\text{joule}} = R_s I^2 + \frac{V_1^2}{R_1} \tag{16}$$

where V_1 is the voltage across R_1 in the single $R-C$ branch.

The inclusion of reversible heat generation in the model which is the second contributor to the total heat generation is required to accurately predict the dynamic temperature response for cycling over different SOC ranges at both low and
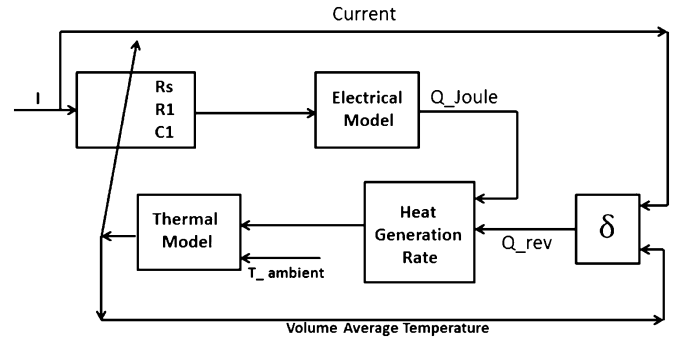

Fig. 12. Coupling of the electrical and thermal models.

Mass (Kg)	Length (m)	Radius (m)	Volume (m^3)	Density (Kgm^{-3})
0.51	0.138	0.0304	4E-4	1277

high currents and temperatures. The reversible (entropic) heat generation rate is governed by [36]

$$Q_{\text{rev}} = \delta \bar{T} I(t). \tag{17}$$

The reversible heat generation rate is proportional to the current and the volume average temperature $\bar{T}$ with the unit of ($°K$) [36]. The constant of proportionality δ is related to the physical properties of the cell, and it will be estimated from the temperature measurements. As an example, Fig. 11 shows the reversible and irreversible heat generation rate profiles for a specific test at 25 °C, 140 A, 90 seconds rest period, and full SOC range. The first two subplots show the applied current profiles and the measured surface temperature. The inset in the heat generation plot at the steady-state region shows that the reversible heat generation rate is proportional to the magnitude and direction of the current, while the irreversible heat generation rate is always positive and almost a linear function of time. Integrating the heat generation rates at steady state for either charging or discharging, the reversible heat generation is calculated to be 616 J compared to the 392 J of the irreversible heat generation. This is an indicator of the significance of including the entropic heat generation in the thermal model.

Considering the ions in the supercapacitor as the system of interest, the change of entropy of this system from state 1 to state 2 is

$$\Delta S = -\int_1^2 \frac{dQ_{\text{rev}}}{T} = -C_p \ln\left(\frac{T_2}{T_1}\right) \tag{18}$$

where C_p is the heat capacitance of the double-layer supercapacitor. Entropy can be interpreted as a measure of disorder in a system. This means that, the higher the level of disorder in a system, the higher the entropy. During charging as the ions move to the surface of the electrodes, the disorder of the system of ions is decreasing; therefore, the entropy decreases. According to (18), for ΔS to be negative (decreasing entropy), T_2 should be greater than T_1, which explains the increase in temperature during charging. While discharging, the level of disorder in ions is increasing as they spread out in the electrolyte randomly, similar to an ideal gas [36]. This results in an increase in the
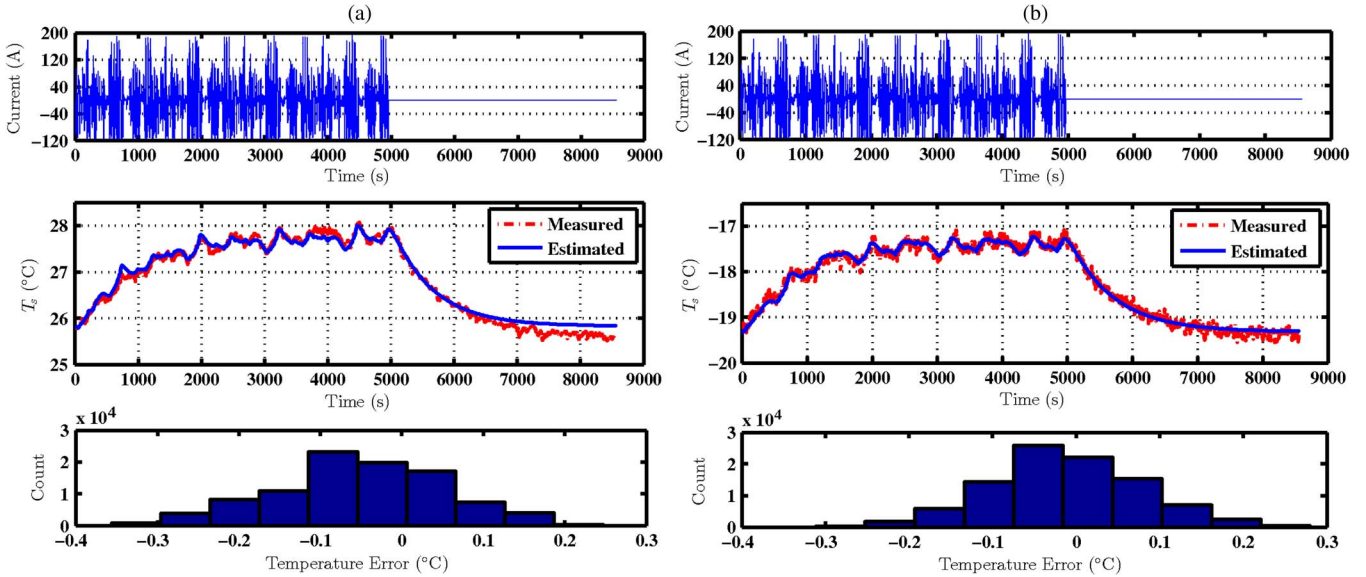
Fig. 13. Thermal model parameterization result using the urban assault driving cycle (UAC) at (a) 25 °C and (b) -20 °C.

entropy $(\Delta S > 0)$, which dictates a decrease in temperature $(T_2 < T_1)$ according to (18), clarifying the observed cooling effect during discharge.

D. Coupling of the Electrical and Thermal Models

Fig. 12 is the schematic of the coupled electrothermal model. The electrical and thermal models are coupled to form the complete system model. The total heat generation rate is calculated from the equivalent circuit model, and the temperature (which is the output of the thermal model) feeds back into the parameters of the equivalent circuit model.

E. Parameterization Results for the Thermal Model

The convective h and conductive k_t heat coefficients, the specific heat coefficient c_p, and the parameter in (17) associated with reversible heat generation δ are the parameters to be identified for the thermal model. The measured surface temperature is used in this study, which is sufficient for parameterization. However, core temperature measurements such as in [52] could also be used for identification and validation purposes. The urban assault cycle (UAC) which is also used to generate the battery current profile for a heavy vehicle [53] is scaled up by a factor of 6 to generate an input current profile with sufficient excitation for supercapacitor applications. Also, a relaxation period of 1 h is added to the end of the experiment, which results in useful temperature relaxation data for parameterizing the heat capacity and coefficient of convective cooling in the model. The physical parameters of the cell that are measurable are summarized in Table III.

Parameter estimation is performed by minimizing the square error between the measured (T_m) and simulated (T_s) surface temperatures. The cost function to be minimized is

$$J = \sum_k \left(T_m(k) - T_s(k)\right)^2. \qquad (19)$$

TABLE IV
IDENTIFIED THERMAL PARAMETERS AT 25 °C
AND -20 °C USING UAC

		h $(\mathrm{Wm^{-2}K^{-1}})$	c_p $(\mathrm{JKg^{-1}K^{-1}})$	k_t $(\mathrm{Wm^{-1}K^{-1}})$	δ $(\mathrm{JCoulomb^{-1}K^{-1}})$
T_∞	25	157	1259	0.49	4E−4
	-20	26	1480	0.74	2.3E−4

Fig. 13 compares the modeled surface temperature with experimental measurements performed on the cell using the UAC duty cycle at 25 °C and subzero temperature of -20 °C. The histogram of the temperature error is also shown for both temperatures. The RMS errors are 0.13 °C and 0.11 °C for 25 °C and -20 °C, respectively, which is an indicator of the estimation accuracy. Table IV shows the values of the identified thermal model parameters for both 25 °C and -20 °C. The value estimated for h is in the range of forced convective heat transfer coefficient for air, which is between 10 and 200 $\mathrm{Wm^{-2}K^{-1}}$. The thermal chamber consists of a fan inside it, which helps regulate the temperature to the preset value. The estimated value of h will depend on the fan being on or off during the experiment, which is the reason for the different values of h at two temperatures of 25 °C and -20 °C. The specific heat coefficient values are close to the amount of the cell's organic-based electrolyte (acetonitrile $c_p = 1863$ $\mathrm{Jkg^{-1}K^{-1}}$ at 25 °C). The thermal conductivity values are a result of the combined thermal conductivity of activated carbon, electrolyte, separator, and aluminum current collectors formed in a jelly roll shape. The value of 4E−4 for δ at 25 °C is comparable to 3.3E−4 reported in [36] for a 2.7-V/5000-F prismatic cell with organic electrolyte at room temperature.

V. ELECTROTHERMAL MODEL VALIDATION

The supercapacitor was tested under a different current profile, the escort convoy cycle (ECC). ECC, which is a current
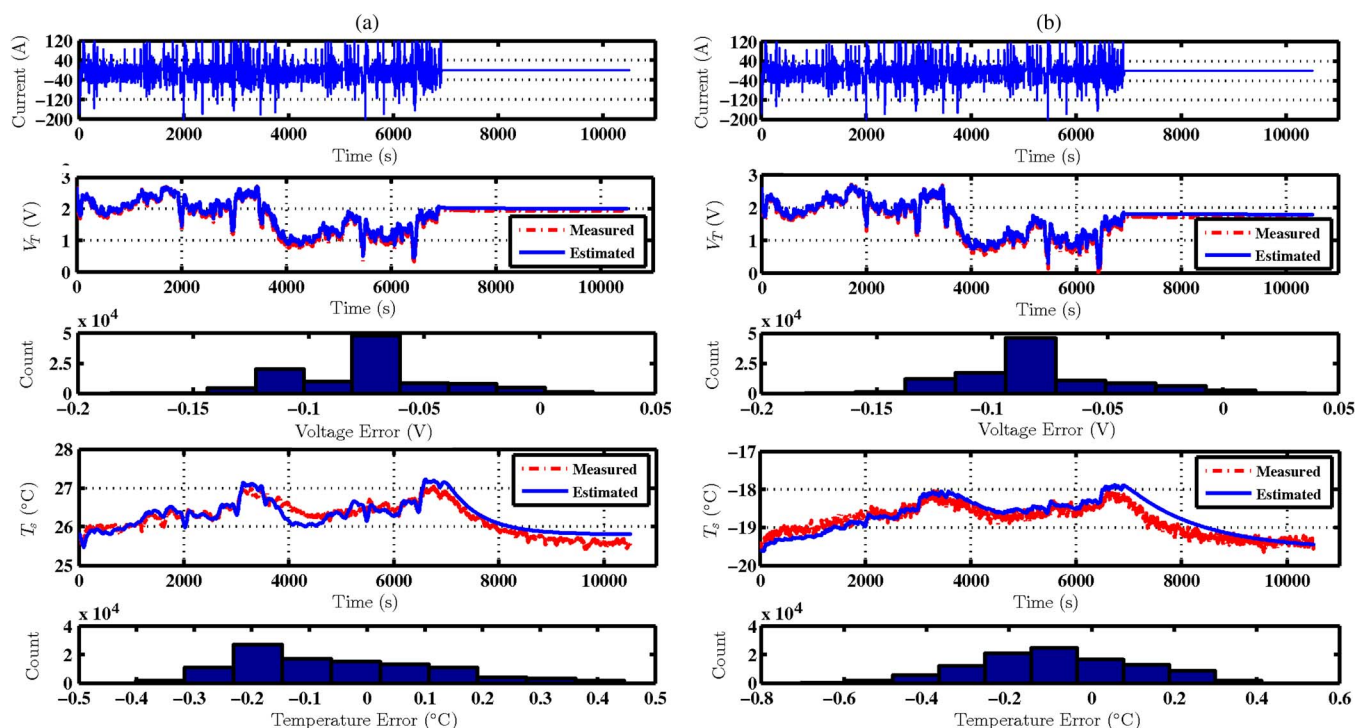
Fig. 14. Electrothermal model validation using scaled ECC current profile at (a) 25 °C and (b) -20 °C.

profile for batteries [48], is scaled up by a factor of 4 and used as the second duty cycle to validate the thermal model and also the electrical model. Under this current profile at 25 °C and -20 °C, the terminal voltage and the surface temperature of the cell are measured. The identified parameters obtained from the parameterization procedures are fixed, and the terminal voltage and surface temperature from the model are compared to the actual measurements. Fig. 14 shows that both electrical and thermal models mimic the actual measurements of the voltage and temperature with good accuracy at both 25 °C and -20 °C. The histograms of the voltage and temperature errors are also shown. The RMS errors for the terminal voltages are 82 and 87 mV for 25 °C and -20 °C, respectively. The surface temperature RMS errors are 0.17 °C for 25 °C and 0.21 °C for -20 °C.

VI. CONCLUSION

In this paper, a computationally efficient electrothermal model has been proposed for a cylindrical supercapacitor. The electrical model was parameterized using pulse-relaxation data from the experiments conducted on the cell. The model is valid from -40 °C to 60 °C considering the dependence of the parameters on temperature, SOC, current direction, and current magnitude. The final electrical model consists of three parameters. The results show that the parameters have a higher dependence on temperature than SOC or current magnitude and direction. The thermal model included the reversible (entropic) as well as the irreversible heat generation. The thermal model consisted of four parameters which were identified using a real-world duty cycle. The coupling between the electrical and thermal models was done by feeding the total heat generation calculated from the electrical model into the thermal model. This allowed the tuning of the temperature-dependent electrical model parame-

ters, according to the temperature dynamics obtained from the thermal model. Finally, the electrothermal model was validated using real-world driving cycles. The validation results show the high accuracy of the proposed electrothermal model which is suitable for real-time implementations in all kinds of power systems and also thermal management of supercapacitor packs.

REFERENCES

[1] T. Strasser *et al.*, "A review of architectures and concepts for intelligence in future electric energy systems," *IEEE Trans. Ind. Electron.*, vol. 62, no. 4, pp. 2424–2438, Apr. 2014.

[2] S. Vazquez, S. M. Lukic, E. Galvan, L. G. Franquelo, and J. M. Carrasco, "Energy storage systems for transport and grid applications," *IEEE Trans. Ind. Electron.*, vol. 57, no. 12, pp. 3881–3895, Dec. 2010.

[3] J. Pegueroles-Queralt, F. D. Bianchi, and O. Gomis-Bellmunt, "A power smoothing system based on supercapacitors for renewable distributed generation," *IEEE Trans. Ind. Electron.*, vol. 62, no. 1, pp. 343–350, Jan. 2015.

[4] H. Zhao, Q. Wu, S. Hu, H. Xu, and C. N. Rasmussen, "Review of energy storage system for wind power integration support," *Appl. Energy*, vol. 137, pp. 545–553, Jan. 2015.

[5] S. G. Jayasinghe and D. M. Vilathgamuwa, "Flying supercapacitors as power smoothing elements in wind generation," *IEEE Trans. Ind. Electron.*, vol. 60, no. 7, pp. 2909–2918, Jul. 2013.

[6] H. Kanchev, D. Lu, F. Colas, V. Lazarov, and B. Francois, "Energy management and operational planning of a microgrid with a PV-based active generator for smart grid applications," *IEEE Trans. Ind. Electron.*, vol. 58, no. 10, pp. 4583–4592, Oct. 2011.

[7] M. Alamir, M. A. Rahmani, and D. Gualino, "Constrained control framework for a stand-alone hybrid (Stirling engine)/supercapacitor power generation system," *Appl. Energy*, vol. 118, pp. 192–206, Apr. 2014.

[8] A. Lahyani, P. Venet, A. Guermazi, and A. Troudi, "Battery/supercapacitors combination in uninterruptible power supply (UPS)," *IEEE Trans. Power Electron.*, vol. 28, no. 4, pp. 1509–1522, Apr. 2013.

[9] A. M. Pernia *et al.*, "Power supply based on carbon ultracapacitors for remote supervision systems," *IEEE Trans. Ind. Electron.*, vol. 57, no. 9, pp. 3139–3147, Sep. 2010.

[10] X. Luo, J. Wang, M. Dooner, and J. Clarke, "Overview of current development in electrical energy storage technologies and the application potential in power system operation," *Appl. Energy*, vol. 137, pp. 511–536, Jan. 2015.

[11] M. Ristic, Y. Gryska, J. V. McGinley, and V. Yufit, "Supercapacitor energy storage for magnetic resonance imaging systems," *IEEE Trans. Ind. Electron.*, vol. 61, no. 8, pp. 4255–4264, Aug. 2014.

[12] C. Park, K. No, and P. H. Chou, "TurboCap: A batteryless, supercapacitor-based power supply for mini-FDPM," *Laser*, vol. 1, pp. 1–8, 2008.

[13] O. Abdel-baqi, A. Nasiri, and P. Miller, "Dynamic performance improvement and peak power limiting using ultracapacitor storage system for hydraulic mining shovels," *IEEE Trans. Ind. Electron.*, vol. 62, no. 5, pp. 3173–3181, May 2015.

[14] W. Greenwell and A. Vahidi, "Predictive control of voltage and current in a fuel cell-ultracapacitor hybrid," *IEEE Trans. Ind. Electron.*, vol. 57, no. 6, pp. 1954–1963, Jun. 2010.

[15] A.-L. Allegre *et al.*, "Energy storage system with supercapacitor for an innovative subway," *IEEE Trans. Ind. Electron.*, vol. 57, no. 12, pp. 4001–4012, Dec. 2010.

[16] S. N. Motapon, L.-A. Dessaint, and K. Al-Haddad, "A comparative study of energy management schemes for a fuel-cell hybrid emergency power system of more-electric aircraft," *IEEE Trans. Ind. Electron.*, vol. 61, no. 3, pp. 1320–1334, Mar. 2014.

[17] Z. Song *et al.*, "Energy management strategies comparison for electric vehicles with hybrid energy storage system," *Appl. Energy*, vol. 134, pp. 321–331, Dec. 2014.

[18] Y. Parvini and A. Vahidi, "Optimal charging of ultracapacitors during regenerative braking," in *Proc. IEEE Int. Elect. Veh. Conf.*, 2012, pp. 1–6.

[19] P. Keil and A. Jossen, "Improving the low-temperature performance of electric vehicles by hybrid energy storage systems," in *Proc. IEEE Veh. Power Propulsion Conf.*, 2014, pp. 1–6.

[20] H. Liu, Z. Wang, J. Cheng, and D. Maly, "Improvement on the cold cranking capacity of commercial vehicle by using supercapacitor and lead-acid battery hybrid," *IEEE Trans. Veh. Technol.*, vol. 58, no. 3, pp. 1097–1105, Mar. 2009.

[21] I. S. Ike, I. Sigalas, S. Iyuke, and K. I. Ozoemena, "An overview of mathematical modeling of electrochemical supercapacitors/ultracapacitors," *J. Power Sources*, vol. 273, pp. 264–277, Jan. 2015.

[22] L. Zubieta and R. Bonert, "Characterization of double-layer capacitors for power electronics applications," *IEEE Trans. Ind. Appl.*, vol. 36, no. 1, pp. 199–205, Jan./Feb. 2000.

[23] N. Bertrand, J. Sabatier, O. Briat, and J.-M. Vinassa, "Embedded fractional nonlinear supercapacitor model and its parametric estimation method," *IEEE Trans. Ind. Electron.*, vol. 57, no. 12, pp. 3991–4000, Dec. 2010.

[24] N. Devillers, S. Jemei, M.-C. Péra, D. Bienaimé, and F. Gustin, "Review of characterization methods for supercapacitor modeling," *J. Power Sources*, vol. 246, pp. 596–608, Jan. 2014.

[25] V. Musolino, L. Piegari, and E. Tironi, "New full-frequency-range supercapacitor model with easy identification procedure," *IEEE Trans. Ind. Electron.*, vol. 60, no. 1, pp. 112–120, Jan. 2013.

[26] D. Torregrossa, M. Bahramipanah, E. Namor, R. Cherkaoui, and M. Paolone, "Improvement of dynamic modeling of supercapacitor by residual charge effect estimation," *IEEE Trans. Ind. Electron.*, vol. 61, no. 3, pp. 1345–1354, Mar. 2014.

[27] N. Rizoug, P. Bartholomeus, and P. Le Moigne, "Modeling and characterizing supercapacitors using an online method," *IEEE Trans. Ind. Electron.*, vol. 57, no. 12, pp. 3980–3990, Dec. 2010.

[28] H. Gualous, D. Bouquain, A. Berthon, and J. Kauffmann, "Experimental study of supercapacitor serial resistance and capacitance variations with temperature," *J. Power Sources*, vol. 123, no. 1, pp. 86–93, Sep. 2003.

[29] S. Buller, E. Karden, D. Kok, and R. W. De Doncker, "Modeling the dynamic behavior of supercapacitors using impedance spectroscopy," *IEEE Trans. Ind. Appl.*, vol. 38, no. 6, pp. 1622–1626, Nov./Dec. 2002.

[30] A. Hijazi *et al.*, "Thermal network model of supercapacitors stack," *IEEE Trans. Ind. Electron.*, vol. 59, no. 2, pp. 979–987, Feb. 2012.

[31] P. Kreczanik, P. Venet, A. Hijazi, and G. Clerc, "Study of supercapacitor aging and lifetime estimation according to voltage, temperature, and RMS current," *IEEE Trans. Ind. Electron.*, vol. 61, no. 9, pp. 4895–4902, Sep. 2014.

[32] H. Gualous, H. Louahlia-Gualous, R. Gallay, and A. Miraoui, "Supercapacitor thermal modeling and characterization in transient state for industrial applications," *IEEE Trans. Ind. Appl.*, vol. 45, no. 3, pp. 1035–1044, May/Jun. 2009.

[33] H. Gualous, H. Louahlia, and R. Gallay, "Supercapacitor characterization and thermal modeling with reversible and irreversible heat effect," *IEEE Trans. Power Electron.*, vol. 26, no. 11, pp. 3402–3409, Nov. 2011.

[34] A. d'Entremont and L. Pilon, "First-principles thermal modeling of electric double layer capacitors under constant-current cycling," *J. Power Sources*, vol. 246, pp. 887–898, Jan. 2014.

[35] A. Berrueta, I. San, A. Hernández, A. Ursúa, and P. Sanchis, "Electro-thermal modeling of a supercapacitor and experimental validation," *J. Power Sources*, vol. 259, pp. 154–165, Aug. 2014.

[36] J. Schiffer, D. Linzen, and D. U. Sauer, "Heat generation in double layer capacitors," *J. Power Sources*, vol. 160, no. 1, pp. 765–772, Sep. 2006.

[37] J. Lee *et al.*, "Modeling of the electrical and thermal behaviors of an ultracapacitor," *Energies*, vol. 7, no. 12, pp. 8264–8278, Dec. 2014.

[38] Y. Parvini, J. B. Siegel, A. G. Stefanopoulou, and A. Vahidi, "Preliminary results on identification of an electro-thermal model for low temperature and high power operation of cylindrical double layer ultracapacitors," in *Proc. IEEE Amer. Control Conf.*, 2014, pp. 242–247.

[39] X. Lin *et al.*, "A lumped-parameter electro-thermal model for cylindrical batteries," *J. Power Sources*, vol. 257, pp. 1–11, Jul. 2014.

[40] H. E. Perez *et al.*, "Parameterization and validation of an integrated electro-thermal cylindrical LFP battery model," in *Proc. ASME Annu. Dyn. Syst. Control Conf.*, 2012, pp. 41–50.

[41] L. Lam, P. Bauer, and E. Kelder, "A practical circuit-based model for Li-ion battery cells in electric vehicle applications," in *Proc. IEEE Int. Telecommun. Energy. Conf.*, 2011, pp. 1–9.

[42] Y. Parvini and A. Vahidi, "Maximizing charging efficiency of lithium-ion and lead-acid batteries using optimal control theory," in *Proc. IEEE Amer. Control Conf.*, 2015, pp. 317–322.

[43] E. Frackowiak and F. Beguin, "Carbon materials for the electrochemical storage of energy in capacitors," *Carbon*, vol. 39, no. 6, pp. 937–950, May 2001.

[44] P.-L. Taberna, C. Portet, and P. Simon, "Electrode surface treatment and electrochemical impedance spectroscopy study on carbon/carbon supercapacitors," *Appl. Phys. A*, vol. 82, no. 4, pp. 639–646, Mar. 2006.

[45] A. Pandolfo and A. Hollenkamp, "Carbon properties and their role in supercapacitors," *J. Power Sources*, vol. 157, no. 1, pp. 11–27, Jun. 2006.

[46] P. Taberna, P. Simon, and J.-F. Fauvarque, "Electrochemical characteristics and impedance spectroscopy studies of carbon–carbon supercapacitors," *J. Electrochem. Soc.*, vol. 150, no. 3, pp. A292–A300, Mar. 2003.

[47] B. E. Conway, *Electrochemical Supercapacitors: Scientific Fundamentals and Technological Applications*. New York, NY, USA: Springer-Verlag, 2013.

[48] Y. Kim, S. Mohan, J. Siegel, A. Stefanopoulou, and Y. Ding, "The estimation of temperature distribution in cylindrical battery cells under unknown cooling conditions," *IEEE Trans. Control Syst. Technol.*, vol. 22, no. 6, pp. 2277–2286, Nov. 2014.

[49] D. H. Jeon and S. M. Baek, "Thermal modeling of cylindrical lithium ion battery during discharge cycle," *Energy Conversion Manag.*, vol. 52, no. 8/9, pp. 2973–2981, Aug. 2011.

[50] H. Maleki, S. Al, J. R. Selman, R. B. Dinwiddie, and H. Wang, "Thermal properties of lithium-ion battery and components," *J. Electrochem. Soc.*, vol. 146, no. 3, pp. 947–954, Feb. 1999.

[51] V. R. Subramanian, V. D. Diwakar, and D. Tapriyal, "Efficient macro–micro scale coupled modeling of batteries," *J. Electrochem. Soc.*, vol. 152, no. 10, pp. A2002–A2008, Jan. 2005.

[52] Y. Kim, "Power capability estimation accounting for thermal and electrical constraints of lithium-ion batteries," Ph.D. dissertation, Univ. Michigan, Ann Arbor, MI, USA, 2014.

[53] T.-K. Lee, Y. Kim, A. Stefanopoulou, and Z. S. Filipi, "Hybrid electric vehicle supervisory control design reflecting estimated lithium-ion battery electrochemical dynamics," in *Proc. IEEE Amer. Control Conf.*, 2011, pp. 388–395.

Yasha Parvini (S'11) received the B.S. degree in mechanical engineering from the University of Tabriz, Tabriz, Iran, in 2006 and the M.Sc. degree in mechanical engineering from Sharif University of Technology, Tehran, Iran, in 2010. He is currently working toward the Ph.D. degree in the Department of Mechanical Engineering, Clemson University, Clemson, SC, USA.

He was a Visiting Graduate Student Researcher at the University of Michigan, Ann Arbor, MI, USA, in 2012–2013. His research interests include modeling, estimation, and control of energy systems, particularly electrical energy storages such as batteries and supercapacitors.

Jason B. Siegel (M'08) received the B.S., M.S., and Ph.D. degrees in electrical engineering systems from the University of Michigan, Ann Arbor, MI, USA, in 2004, 2006, and 2010, respectively.

He is currently an Assistant Research Scientist with the Department of Mechanical Engineering, University of Michigan. His research areas focus on modeling and simulation of electrochemical energy storage and conversion for the design of control systems.

Anna G. Stefanopoulou (F'09) received the Diploma from the National Technology University of Athens, Athens, Greece, in 1991, and the M.S. degree in naval architecture and marine engineering and the M.S. and Ph.D. degrees in electrical engineering and computer science from the University of Michigan, Ann Arbor, MI, USA, in 1992, 1994, and 1996, respectively.

She is a Professor of mechanical engineering and the Director of the Automotive Research Center, University of Michigan, Ann Arbor, MI, USA. From 1996 to 1997, she was a Technical Specialist with Ford Motor Company, Dearborn, MI. From 1998 to 2000, she was an Assistant Professor with the University of California, Santa Barbara, CA, USA. She is the author or coauthor of more than 200 papers and a book on estimation and control of internal combustion engines and electrochemical processes, such as fuel cells and batteries. She is the holder ten U.S. patents.

Prof. Stefanopoulou is a Fellow of the American Society of Mechanical Engineers. She was a recipient of five best paper awards.

Ardalan Vahidi (M'01) received the B.S. and M.Sc. degrees in civil engineering from Sharif University, Tehran, Iran, in 1996 and 1998, respectively, the M.Sc. degree in transportation safety from George Washington University, Washington, DC, USA, in 2002, and the Ph.D. degree in mechanical engineering from the University of Michigan, Ann Arbor, MI, USA, in 2005.

He is currently an Associate Professor with the Department of Mechanical Engineering, Clemson University, Clemson, SC, USA. He was a Visiting Scholar at the University of California, Berkeley, CA, USA, and a Visiting Researcher at the BMW Group Technology Office USA in 2012–2013. His current research interests include control of vehicular and energy systems and connected vehicle technologies.